H and CO Co-induced Roughening of Cu Surface in CO_2 Electroreduction Conditions

Zisheng Zhang,[a] Winston Gee,[a] Philippe Sautet,[a,b,c,*] Anastassia N. Alexandrova[a,c,d,*]

[a] Department of Chemistry and Biochemistry, University of California, Los Angeles, CA 90094, USA

[b] Department of Chemical and Biomolecular Engineering, University of California, Los Angeles, CA 90094, USA

[c] California NanoSystems Institute, University of California, Los Angeles, CA 90094, USA

[d] Department of Materials Science and Engineering, University of California, Los Angeles, CA 90094, USA

ABSTRACT

The dynamic restructuring of Cu has been observed under electrochemical conditions, and it has been hypothesized to underlie the unique reactivity of Cu towards CO_2 electroreduction. Roughening is one of the key surface phenomena for Cu activation, whereby numerous atomic vacancies and adatoms form. However, the atomic structure of such surface motifs in the presence of relevant adsorbates has remained elusive. Here, we explore the chemical space of Cu surface restructuring under coverage of CO and H in realistic electroreduction conditions, by combining grand canonical DFT and global optimization techniques, from which we construct a potential-dependent grand canonical ensemble representation. The regime of intermediate and mixed CO and H coverage—where structures exhibit some elevated surface Cu—is thermodynamically unfavorable yet kinetically required. Therefore, we develop a quasi-kinetic Monte Carlo simulation to track the system's evolution during a simulated cathodic scan. We reveal the evolution path of the system across coverage space and identify the accessible metastable structures formed along the way. Chemical bonding analysis is performed on the metastable structures with elevated Cu*CO species to understand their formation mechanism. By molecular dynamics simulations and free energy calculations, the surface chemistry of the Cu*CO species is explored, and we identify plausible mechanisms via which the Cu*CO species may diffuse or dimerize. This work provides rich atomistic insights into the phenomenon of surface roughening and the structure of involved species. It also features generalizable methods to explore the chemical space of restructuring surfaces with mixed adsorbates and their non-equilibrium evolution.

INTRODUCTION

In the quest for a sustainable future, electrocatalysis stands as a cornerstone, driving the electrochemical storage of renewable energy and paving the way for the production of valuable molecules from waste and greenhouse gases. Knowledge of the surface structure under reaction conditions is central to electrocatalyst development, as it is the prerequisite to mechanistic investigation and subsequent optimization. However, the more we know, the more we realize we don't know – with improving resolution of surface characterization techniques, it increasingly becomes evident that the electrocatalytic surfaces are not static landscapes. Instead, they are dynamic arenas where an ensemble of catalyst states fight in chaos, with a diverse distribution of geometry, composition, and reactivity.[1,2]

Copper, the only transition metal that efficiently catalyzes CO_2 reduction reaction (CO_2RR) into C_{2+} multi-electron reduction products,[3] is intriguingly notorious for undergoing complex redox and structural dynamics under electrochemical conditions.[4,5] From bulk phase transition to surface reconstruction,[6] and from dissolution-redeposition to nanoclustering,[7,8] the fluxional nature of Cu electrocatalysts seem to underpin their unique reactivity. A surface species key to the abovementioned phenomena is the Cu adatom, whose existence has been confirmed in CO_2RR and CO electro-oxidation conditions.[9,10] Multiple structural models of the adatom have been proposed, but most of them were built based on experimental signals and speculations, or neglected the many realistic aspects.[9,11,12] The atomic structure and formation mechanisms of these surface adatoms, under the effect of electrode potential and surface adsorbates, is still lacking.

As a sequel to our previous efforts to understand the H-induced restructuring of Cu(100)[13] and Cu(111)[14] in electroreduction conditions, here we investigate the case where the surface is under a mixed coverage of both *H and *CO, which is more relevant to CO_2RR and CO electro-reduction/oxidation reactions. By performing grand canonical genetic algorithm (GCGA) global optimization and grand canonical density functional theory (GCDFT) calculation, we constructed potential-dependent grand canonical ensemble and free energy landscapes of Cu surfaces under different coverages of *H and *CO. Due to the failure of Boltzmann statistics in predicting any changes to the Cu surface morphology, we devised a pseudo-kinetic Monte Carlo simulation to address the non-equilibrium nature of the system and to identify the metastable states that the system would be trapped into under reducing potentials. A number of Cu*CO species, which are

elevated from the top surface under the co-influence of atop *CO and surrounding *H, were predicted to form in the CO_2RR-relevant potential regime. The chemical bonding origin of the H and CO co-induced formation of elevated Cu*CO species is investigated, and the possible pathways for surface migration and dimerization of the formed elevated Cu*CO are probed by free energy calculations. This study provides rich insights into the formation and chemistries of the roughened Cu surfaces in realistic electrochemical conditions, which can benefit the electrocatalysis community in mechanistic investigations and further optimization of Cu electrocatalysts.

RESULTS & DISCUSSION

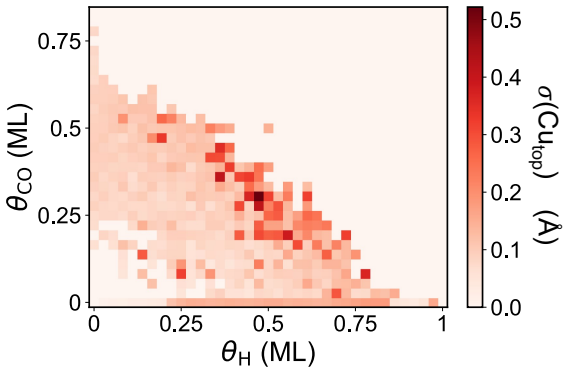

Figure 1. Vertical displacement of surface Cu atoms as a function of CO and H coverages, for the global minimum structure of each coverage state, without applied potential. Darker color indicates a larger standard deviation in the heights of top surface Cu atoms in the top monolayer of the surface.

We consider the Cu surfaces to be under the coverage of both CO and H, which are the two main reaction intermediates in CO_2RR in near-neutral or acidic conditions. Due to the extremely large chemical space spanned by surface rearrangement and mixed adsorbate coverage, grand canonical genetic algorithm (GCGA)[13,15–17] is used to globally optimize the configuration of Cu(100), (111), and (711) step under the coverage of both H and CO (Methods and Supplementary Note 1 for details). To be specific, the system is allowed to exchange H and CO with a reservoir with fixed chemical potentials of H and CO (μ_H and μ_{CO}), so that the search direction in the compositional space will be self-adaptive. To cover the chemically relevant range of μ_H and μ_{CO}, multiple GCGA searches are performed at a pH of 7, CO partial pressure of 1 atm, and electrode potentials between 0 and -1 V_{SHE}.

In total, 16,830, 22,511, and 20,555 unique catalyst states are obtained for Cu(100), Cu(111), and Cu(711), respectively. The main body of this work will be focusing on the reconstruction of Cu(100), which has well-studied H-induced restructuring and chemistry in previous theoretical and experimental works,[13,14,18] while the others share similar adsorbate-induced reconstructing behaviors (Figure S3).[19] All three collections well cover the regime of mixed H and CO adsorption up to 1 ML H and 0.75 ML CO, with a quite broad distribution of geometries. Figure 1 shows the standard deviation of top surface Cu atoms' heights as a function of H coverage and

CO coverage, which represents the extent of structural rearrangement on the top monolayer of the surface. Under the coverage of only CO, the Cu surface stays in the pristine (100) configuration. Under coverage of only H, shifted-row configurations can form only at higher H coverages, which is consistent with our previous findings.[13] Neither H-only, nor CO-only coverage can induce any significant vertical displacement of surface atom at a constant surface density of Cu.[14] However, at an intermediate coverage of both H and CO, many catalyst states with elevated atoms become accessible. This can be seen from the much larger standard deviations of Cu (reaching 0.5 Å), in the region with CO coverage from 0.2 to 0.5 ML and H coverage from 0.3 to 0.7 ML.

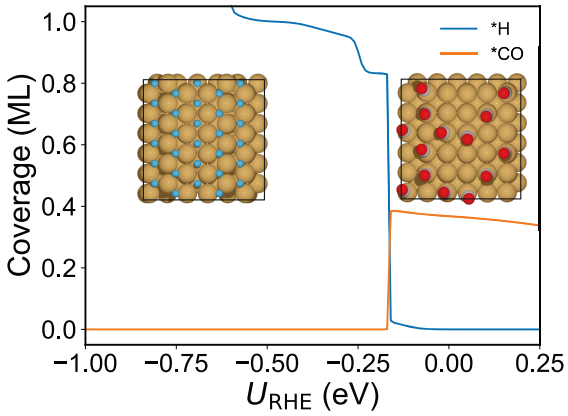

Figure 2. CO and H coverage as functions of electrochemical potential from Boltzmann statistics. Representative structure of H-only and CO-only coverage structures are shown as insets.

To assess the relative accessibility of the identified structures under the applied bias, we performed grand canonical density functional theory (GCDFT) calculations on the low-energy local minima (LELM) for each adsorbate coverage to construct a grand canonical ensemble of H, CO, and electrons. This approach makes possible a comparison of potential-dependent thermodynamic stability for the states in the ensemble, according to grand canonical free energetics. To study the evolution of the surface structure under varying electrochemical potentials, we first apply Boltzmann statistics to calculate the population of the states in the

ensemble, solely based on thermodynamics (Figure 2). The surface Cu arrangement is predicted to stay pristine near zero applied potential with CO coverage of about 0.4 ML and no H. It rearranges into the doubly shifted-row configuration, a pure surface hydride phase, at more negative potentials with H coverage of about 1 ML and no CO. However, the jump in adsorbate coverage from CO-only to H-only states is abrupt – the transition is δ-function like, and occurs within a very narrow potential window, skipping all mixed coverage states. From the point of view of the mechanism of surface reconstruction and its dynamics, this abrupt change appears rather unphysical. In addition, the doubly row-shifted configuration has been experimentally shown to be inaccessible at pH>3, regardless of how negative the potential is, due to kinetic limitations.[20] Considering the near-neutral pH and presence of CO (competing adsorbate) in CO_2RR conditions, the system of this study should suffer even stronger kinetic hinderances and be unable to build up a high enough H coverage to form doubly shifted-row configuration, dihydrogen ligand,[14] or sub-surface H.[13]

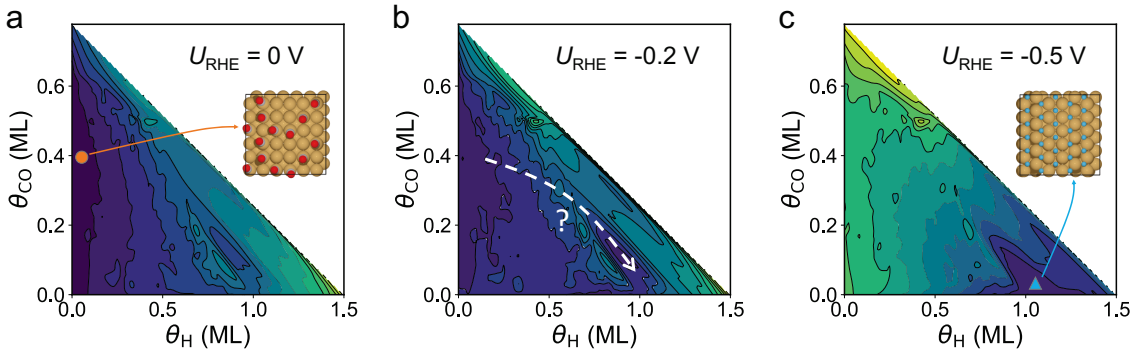

Figure 3. Grand canonical free energy surfaces as functions of H and CO coverages, at electrochemical potentials of (a) 0 V, (b) -0.2 V, and (c) -0.5 V, in RHE scale. Dark blue and light yellow colors represent low and high free energies, respectively.

The unphysical "coverage jump" behaviour in the thermodynamic picture prompt us to look into the detailed evolution of the free energy landscape in the coverage space as potential varies. At 0 V_{RHE}, the global minimum (GM) and LELMs all lie in the region corresponding to CO-only coverage (Figure 3a). As the potential shifts to -0.2 V_{RHE}, the region of low CO coverage and high H coverage becomes as thermodynamically competitive as the CO-only region (Figure 3b). At -0.5 V_{RHE}, the H-only region contains the GM. The "coverage jump" corresponds to a critical

electrochemical potential where the high H coverage states tie with the high CO coverage states (Figure 3c). After a tiny increment of reducing potential, the high H coverage states outcompete the high CO coverage states in terms of free energy and become the new GM. As a result, the thermodynamic-only picture would predict a sudden inversion of H and CO coverages on the surface. However, in reality, changes in coverage should be continuous and differential, with the surface gaining, losing, or displacing one or few adsorbate(s) at a time, rather than all at once. In other words, when the system is traversing the free energy landscape, its moves are kinetically limited to neighboring coverage states, making it a non-equilibrium phenomenon and undermining the Boltzmann statistics (which would be achievable at infinitely long times). When the system evolves from the initial GM (CO-only coverage) to the new GM (H-only coverage), it is bound to visit a series of coverage states along the way. Such progression can be kinetically hindered due to the bumpy and multi-minima nature of the free energy landscape, causing the system to be stranded, and even trapped, in a relatively flat metastable regime of mixed coverage of H and CO.

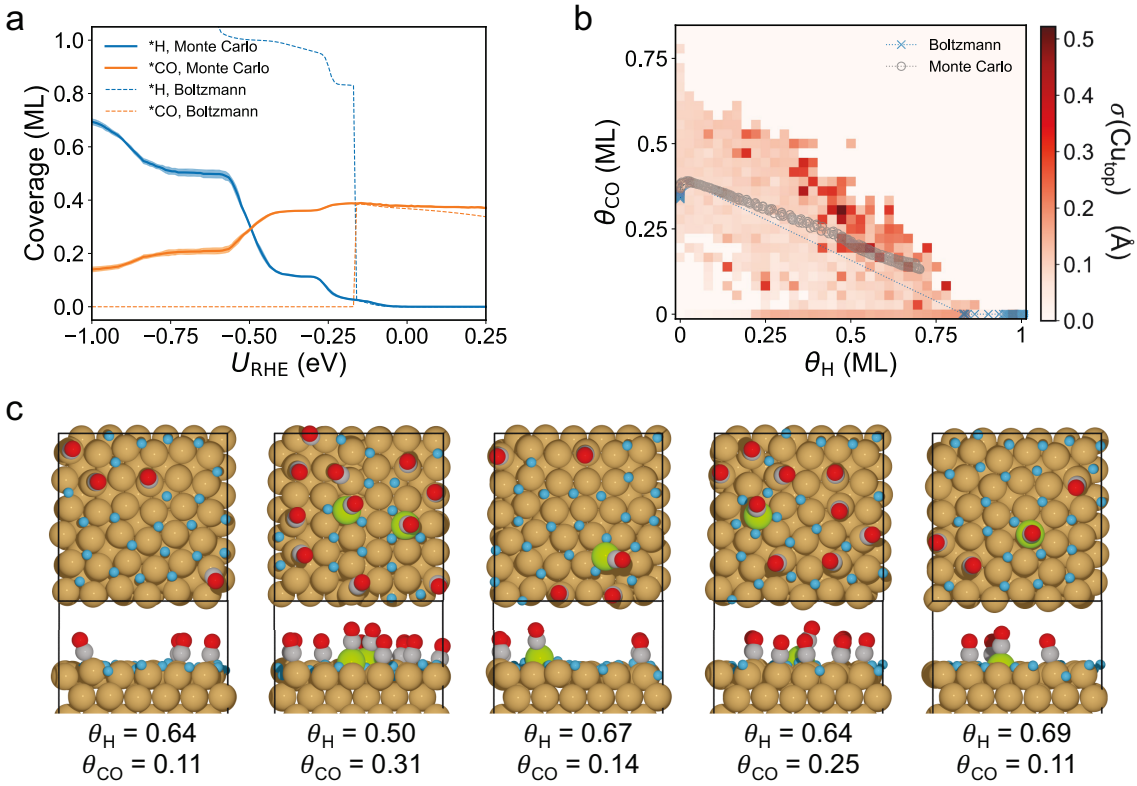

Figure 4. Quasi-kinetic Monte Carlo simulations of surface structure and coverage evolution. (a) H and CO coverages as functions of electrochemical potential, from Boltzmann statistics (dashed lines) and Monte Carlo simulations (solid lines) with error bands. (b) Evolution of the system's coverage state on the vertical displacement map of surface atoms, with respect to H and CO coverages, during a simulated cathodic scan, from Boltzmann statistics (as blue crosses) and Monte Carlo simulations (as red circles). (c) Notable structures (with a maximum population of at least 10%) illustrating significant surface Cu rearrangements under mixed coverage of H and CO. Color code: Cu – brown; H – blue; C – grey; O – red; elevated Cu – green.

To identify the states that the system would visit along its way across the 2-dimensional coverage space, we devise a quasi-kinetic Monte Carlo (MC) simulation to investigate the surface changes under varying electrochemical potential. The surface is represented by a 10×10 lattice of the cells (each of the same size as in GCGA sampling, i.e. an overall 60×60 surface model). Two types of moves (Scheme S1) are considered to represent the electrolyte-electrode and intra-electrode exchange of adsorbates: (i) desorb or adsorb one adsorbate; (ii) displace one adsorbate to a neighboring cell. The kinetic barriers of these moves are assumed to scale with their associated grand canonical free energy changes, which introduces potential dependence and a sense of time into the simulation. During the simulated cathodic scan, the electrode potential is changed in a small increment of 10 mV. At each potential, the system undergoes a finite number of simulation steps (2 million, corresponding to the timescales of microseconds, see Supplementary Note 3), which is sufficient to bring the system to a quasi-equilibrium, but not guaranteeing it to reach the global minima.

The MC simulation presents a completely different picture from the thermodynamic one. The majority adsorbate in the beginning, CO, will still be replaced by H as the potential scans to more negative, but the onset of such crossover is at a much more negative potential (about 0.2 V_{RHE} for Boltzmann; about 0.5 V_{RHE} for MC), and the transition is much smoother than in the thermodynamic-only picture (Figure 4a). Even at very negative potentials, the system never goes

into the H-only coverage state, suggesting trapping in a metastable LM regime without reaching the GM. This is consistent with the experimental observation that CO retains to the surface with a coverage of 0.1 – 0.3 ML during CO_2RR, even at more negative potentials.[21–23]

The path in the coverage space, as the system traverses the potential-dependent free energy landscape, is plotted on the structural deviation map (as in Figure 1) in Figure 4b. The Boltzmann picture predicts an abrupt jump from CO-only to H-only coverage, whereas MC predicts a smooth, continuous path from CO-only coverage into the region of roughly 0.2 ML CO coverage and 0.6 ML H coverage. Note that this path across the coverage space is independent from the scan rate used in the simulation, which indicates that the simulated system is sufficiently relaxed to reveal the intrinsic minimum path on the potential-dependent free energy surface (see Supplementary Note 4).

More interestingly, the observed regime of mixed coverage coincides with the production of elevated Cu*CO species on the surface (Figure 4c). By tracking the statistics of states in the Monte Carlo simulations, we could obtain the population of each state in the metastable regime during the simulated cathodic scan (Figure S8). Starting at about -0.45 V_{RHE}, there is a significant replacement of CO by H on the surface, leading to a *p4g*-like surface arrangement of Cu.[24] In the range of -0.5 to -0.7 V_{RHE}, multiple surface phases with Cu*CO species gain population up to 30%, which are shown in Figure 4c and ordered by onset potential (from positive to negative). The arrangement of surface Cu are primarily in the *p4g*-like configuration, with minority in the singly shifted-row configuration. The overall population of elevated Cu*CO peaks (up to about 50%) in the coverage range of 0.50 to 0.64 ML for H and 0.14 to 0.31 for CO. The elevation of the Cu*CO species decreases at a higher H-to-CO coverage ratio, due to the depleted CO coverage and strong stabilization of in-plane Cu configurations at very high H coverage.[13,14] The system never makes it to the doubly shifted-row hydride phase (the thermodynamic GM with about 1 ML H-only coverage) during simulated cathodic scans of any scan rate within the affordable time scale. The inaccessibility of the deep hydride phase is again consistent with the observations in ref.[20] To probe whether these surface phases could survive a long-term electrolysis or chronoamperometry, we scan the system to a CO_2RR-relevant target potential (-0.6, -0.7, and -0.8 V_{RHE}) where Cu*CO is populated, and then hold the potential constant for a long time scale of 400 million moves. Surprisingly, the Cu*CO-containing phases does not lose but gain population during the constant-potential simulation, with the total

population of Cu*CO-containing phases reaching almost half a monolayer (corresponding to 2% surface concentration of Cu*CO species) at -0.8 V_{RHE}. This suggests that the insufficient relaxation during the simulated cathodic scans in fact underestimates the population of Cu*CO species. A longer time scale would likely populate more Cu*CO in the CO_2RR-relevant potential regime. More details and discussions of the constant-potential simulation are in Supplementary Note 5.

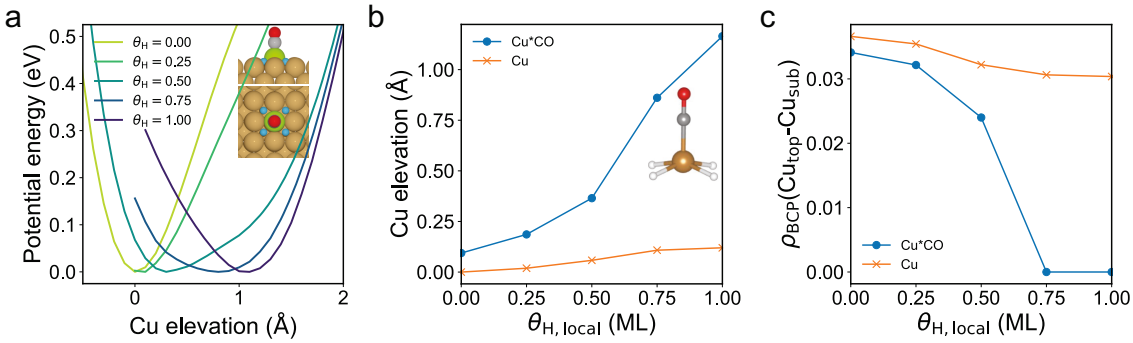

Figure 5. Chemical bonding analysis of the elevated Cu*CO species. (a) Potential energy surface of the Cu elevation with atop CO at different local H coverages. (b) Cu elevation in the minima structures with CO (blue) and without CO (orange) at different local H coverages. (c) Electron density at the bond critical points of Cu_{top}-Cu_{sub} bonds with CO (blue) and without CO (orange) at different local H coverages.

Next, we investigate the electronic structure origin of the formation of elevated Cu*CO species. Due to the complexity and diversity of the local environment of Cu*CO species in the mixed coverage states, we approach it by using a minimal model of pristine Cu(100) with one Cu with or without CO and H adsorbates in different local coverages. We first focus on a top surface Cu with an atop CO and 0 to 4 H surrounding it, corresponding to a local H coverage of 0 to 1 ML. The potential energy surface (PES) of the Cu atom moving in vertical direction out of the surface is obtained by a relaxed scan (Figure 5a). When there is no H in the vicinity of the Cu*CO, the minimum of the PES is at 0.09 Å relative to the bare pristine surface, showing a negligible elevation. The position of the minima and the shape of the PES stays about the same at 0.25 ML local H coverage. As the local H coverage around the Cu*CO further increases, the PES becomes

flatter, and the minimum shifts to a higher elevation. At a local H coverage of 0.75 ML, the minimum shifts to a 0.86 Å elevation, and it further increases to 1.17 Å at 1 ML local H coverage, corresponding to formation of the elevated Cu*CO species. Note that this H-induced elevation of top surface Cu is only significant with an atop CO adsorbate – if without CO, the maximal elevation is merely 0.12 Å at 1 ML local H coverage (Figure 5b). In summary, there is not a kinetic barrier associated with the Cu elevation on any of the fixed-composition PES's, but rather, the minimum of the PES evolves as the local H coverage increases, naturally bringing the Cu*CO to the elevated state at higher local H coverage.

The evolution of the PES shape is also quite intriguing: the PES becomes flatter when local H coverage increases from 0 to 0.75 ML, but it gets steeper again at 1 ML. The coverage-dependent flatness of the PES suggests the presence of two competing interactions, one to hold Cu in-plane and another to drag it out-of-plane. They strike a balance at 0.75 ML local H coverage, marking a critical point for the transition to the elevated state. The elevated Cu*CO formation indeed resembles a phase transition process, which takes place in the local H coverage range of 0.5 to 0.75 ML. This is accompanied by the breaking of chemical bonds between top surface Cu and subsurface Cu atoms, as quantum theory of atom in molecule (QTAIM) analysis suggests in Figure 5c. Note that H merely acts as a "lubricant" which partially weakens the Cu_{top}-Cu_{sub} bonds.[13] The elevated state with a distorted pyramidal configuration, with electron localization and molecular-like characteristics (Supplementary Note 6), can only be stabilized in the presence of an atop CO adsorbate.

The elevated Cu*CO species is unlikely to be the ultimate CO_2RR-active species, but a precursor of them. It has been experimentally observed that the initial roughening, which corresponds to the formation of Cu*CO species, occurs in the activation stage and does not correspond to the steady state of the catalyst.[10] The eventual CO_2RR active sites are expected to be found within (sub)nanoclusters,[9] islands,[25] holes,[26] and/or other surface defects/patterns[27] that result from diffusion and agglomeration of the Cu*CO species.

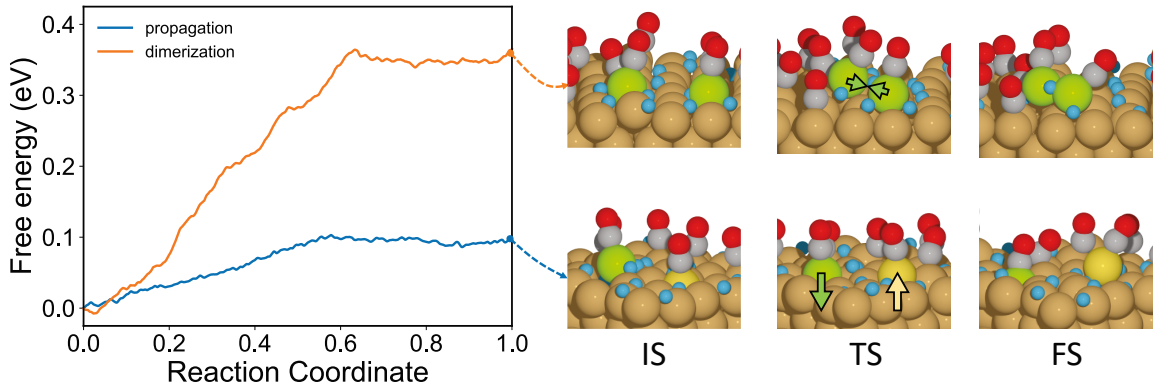

Figure 6. Free energy profiles of Cu*CO propagation and dimerization.

To bridge the gap between atomic Cu*CO species and larger scale surface patterns, we study the propensity of the Cu*CO species to further evolve by dynamic simulations. Since the H adsorbates are highly mobile, and the Cu_{top}-Cu_{sub} bond strengths depend heavily on the local H coverages, we perform molecular dynamics (MD) simulations on the selected catalyst states in Figure 4. In the timescale of a few picoseconds, the Cu*CO species decorated with co-adsorbed H's does not move laterally. However, for some Cu*CO species, we observe an unusual and coupled set of motions: the initially-elevated Cu*CO can sink back into the top surface layer, and another in-plane Cu (a second nearest neighbor of the former one) with atop CO can pop out of the surface, to form a newly-elevated species. In other words, we see a wave-like propagation of the elevated Cu*CO species across the surface.

Since this event is rather rare during regular MD, we perform slow-growth sampling (see Methods and Supplementary Note 7 for details) to obtain the free energy profile of the propagation, with the height of the initial Cu*CO as the reaction coordinate. As the initial Cu*CO presses back into the top surface layer, another surface Cu with atop CO in the second coordination sphere pops up, effectively propagating the Cu*CO over the surface. The barrier of this indirect diffusion process is as low as 0.10 eV, which is feasible at room temperature and is expected to be the major migration pathway of the elevated Cu*CO, rather than direct diffusion. The little kinetic hinderance of this process likely originates in the dynamics of adjacent H adsorbates that accompanies the Cu*CO propagation. To be specific, among the three H adsorbates that directly bond to the initially-elevated Cu*CO, the H closest to the later-elevated Cu*CO diffuses towards, and eventually binds to, the latter, breaking away from the initially-

elevated Cu*CO as it sinks back into the top surface (Figure S13a). In the meantime, the H farthest from the later-elevated Cu*CO also breaks off and diffuses in the opposite direction, away from the initially-elevated Cu*CO, and stabilizes itself at a three-fold hollow site. Both initially- and newly-elevated Cu*CO share a similar coordination environment, binding to three H adsorbates below that are supported on a pentagonal local arrangement of surface Cu (Figure S13b-c). The diffusion of H adsorbate configurations is an indispensable part of the propagation process, as the local arrangement of the H determines the free energy landscape of Cu*CO (not a simple barrier-lowering effect), in a highly coupled manner.

When the elevated Cu*CO diffuses over the surface, it would eventually run into other elevated Cu*CO, and possibly seed islands and clusters.[9,10,25,26] Hence, we further calculate the free energy profile of two Cu*CO interacting with each other, with the inter-Cu distance as the reaction coordinate. The obtained mechanism involves one of the Cu*CO rising from its initial elevated site and hop to a neighboring hollow site, in order to get closer to the other Cu*CO and dimerize (Figure 6). In the end, the two Cu*CO form an OC*Cu-Cu*CO dimer. This process has a significantly higher barrier of 0.36 eV, due to the need for one Cu*CO to break away from its initial surface site. As a result, dimerization is expected to be much less frequent than diffusion, but the barrier should still be crossable at room temperature. The dimerization is also facilitated by local H arrangements (Figure S14): the H adsorbate in between the two Cu*CO's firstly hops from the initial site to a metastable out-of-plane bridge site, so that it can attract and coordinate to both Cu*CO's, drawing them closer to each other. As the two Cu*CO's get close enough and dimerize, the in-between H sinks back to a distorted hollow site and act as a supporting ligand from below, shared by both Cu atoms in the OC*Cu-Cu*CO dimer. This could be the underlying mechanism of Cu clustering and island formation on Cu electrodes in CO_2RR conditions.

In the end, we would like to briefly discuss the reactivity implications of this work. A typical CO_2RR could be broken down to multiple stages: (i) before reaching the CO_2-to-CO onset potential, due to the absence of CO in the reaction system, there should be only hydrogen evolution reactions (HER). In fact, atomically ordered low-index crystalline Cu surface prefer HER over CO_2RR.[28] (ii) When the CO_2-to-CO onset potential is reached (at -0.5 to -0.6 V_{RHE}), CO begin to get electrogenerated, but its concentration level would be too low to induce any major surface restructuring,[22] and HER is still dominant. (iii) At more negative potentials (up to -1.0 V_{RHE}), as the CO coverage builds up on the surface, the system enters the mixed intermediate

coverage regime where Cu*CO – and subsequent (sub)nanostructures or defects – start to form. These structures are the major contributors to the overall turnover, improving the selectivity towards CO_2RR. (iv) When the potential scans to more negative than -1.0 V_{RHE}, the surface would gradually have CO replaced by H and form hydride-like motifs, which should stop (or even reverse, depending on the condition and time scale) Cu*CO formation or subsequent (sub)nanostructuring, with HER coming back to dominance. The deductions qualitatively agree with the experimental selectivity trend on crystalline Cu electrode during a cathodic scan in near neutral media, where the Faradaic efficiency of CO_2RR first increase and then decline after peaking between -1.0 and -1.1 V_{RHE}.[29]

A more quantitative reactivity study (product distribution, C_{2+} selectivities, etc.) needs to be based on the understandings of the Cu*CO-derived (sub)nanostructures, especially their atomic structure, formation mechanism, and lifetime. The highly off-equilibrium nature of the system poses a grand challenge for both experiment (temporal, spatial, and site-specific resolution) and theory (large system size, vast chemical space, long time scale, complex reaction networks, electrolyte dependencies) and calls for more research in these critical aspects.

CONCLUSIONS

In this work, we extensively explore the chemical space of Cu surface restructuring under mixed coverage of H and CO using a grand canonical global optimization technique, and construct a grand canonical ensemble representation of the surface in electrochemical conditions. The surface is predicted to significantly roughen under intermediate coverages of both H and CO; however, the potential dependence of the restructuring is not well described by Boltzmann statistics, as the system is not at equilibrium. A quasi-kinetic Monte Carlo method is developed to simulate the evolution of the surface under varying reducing potentials, with kinetic trapping considered. The "path" of the system across the metastable regime is identified, as well as the accessible reconstructed structures along the way. Under intermediate coverages of both H and CO, elevated Cu*CO species can emerge; they are lifted above the top surface by about 1 Å, are not "adatoms" in a strict sense, and create no immediate vacancies. Chemical bonding analysis reveals the origin of the elevated Cu*CO species to be the combined effects of surface Cu-Cu bond weakening by H and atop coordination of the strong ligand CO. Molecular dynamics simulation and free energy calculations are performed to investigate the further evolution of the Cu*CO species. We found that it can readily diffuse over the surface via a novel propagation mechanism where one Cu*CO sinks back into the top surface and another Cu*CO unit pops up, creating a standing wave. Two Cu*CO may also dimerize with a slightly higher barrier, which is likely the underlying mechanism of further clustering and island formation. This work provides atomic insight into the roughening behavior of Cu electrocatalysts and a way to address complex restructurings that are induced by coverage of mixed adsorbates and far from equilibrium. The overall high surface dynamism, with facile propagation of Cu*CO in the presence of H, raises a question of relevant active site(s) for CO_2RR forming transiently.

METHODS

1. Model Set-up

The Cu(100) surface is modeled by a 4-layer 6×6 supercell of Cu(100) termination with a cell dimension of 15.336 Å×15.336 Å (constructed with experimental lattice parameter from ref [30]). The bottom two layers of the slab are constrained as bulk region, and everything else is allowed to relax as the interface region. A vacuum slab of 15 Å thickness is added in the z-direction to avoid spurious interactions between periodic images.

2. DFT calculations

The local optimizations and energy evaluation are performed with the RPBE functional[31] and PBE_PAW pseudopotentials[32] using the VASP program (version 5.4.4).[33–36] The convergence criteria for electronic and force minimization are set to 10^{-5} eV and 0.05 eV/Å during the global optimization and 10^{-6} eV and 0.01 eV/Å for the final refinement. Due to the relatively large system and sampling size, only the Γ *k*-point is sampled in the reciprocal space of the Brillouin zone throughout, and the cutoff energy for the kinetic energy of the plane-waves was 400 eV.

The transition states (TS) are located using climbing image nudged elastic band (CI-NEB) method[37] with image dependent pair potential (IDPP) interpolation.[38] Each TS geometry has been confirmed to have only one imaginary mode.

All electronic structure analyses are performed based on converged charge density or wavefunction. The Bader charges are calculated using Bader Charge Analysis program.[39] The QTAIM analysis is performed using the critic2 program using the Wigner-Seitz method with a subdivision level of 2.[40]

3. Grand Canonical Genetic Algorithm

To sample the chemical space of both Cu restructuring and adsorbate (H and CO) coverage/configuration, we performed global optimization using the grand canonical genetic algorithm (GCGA) as implemented in our open-source GOCIA python package (https://github.com/zishengz/gocia), which now supports mixed and polyatomic adsorbates. To

be specific, the system is treated as a grand canonical ensemble of H and CO adsorbates, and the search target is to minimize the coverage-dependent grand canonical free energy Ω_{ads}:

$$\Omega_{\mathrm{ads}} = U - TS - \sum \mu_i N_i \approx E^{\mathrm{slab}-n\mathrm{H}} - E^{\mathrm{slab}} - n_{\mathrm{H}} \cdot \mu_{\mathrm{H}}(\mathrm{pH}, U, T) - n_{\mathrm{CO}} \cdot \mu_{\mathrm{CO}}(p_{\mathrm{CO}}, T) \quad (1)$$

Where the $E^{\mathrm{slab}-n\mathrm{H}}$ and E^{slab} are electronic energies of the adsorbate-covered and the bare Cu(100) slab. The vibrational contributions to free energy by the slab atoms are neglected considering their small contribution and high computational cost.[41] The chemical potential of H and of CO, μ_{H} and μ_{CO}, are calculated by:

$$\mu_{\mathrm{H}}(\mathrm{pH}, U, T) = \frac{1}{2} E_{\mathrm{H_2}}^{\mathrm{gas}} - \ln(10)\, k_{\mathrm{B}} T \mathrm{pH} - |e| U_{\mathrm{SHE}} + \left(\mathrm{ZPE}^{\mathrm{gas}} + C_p^{\mathrm{gas}} - TS^{\mathrm{gas}}\right) - \left(\mathrm{ZPE}^{\mathrm{ads}} + C_p^{\mathrm{ads}} - TS^{\mathrm{ads}}\right) \quad (2)$$

$$\mu_{\mathrm{CO}}(p_{\mathrm{CO}}, T) = \frac{1}{2} E_{\mathrm{CO}}^{\mathrm{gas}} + k_B T \ln \frac{p_{\mathrm{CO}}}{p^0} + \left(\mathrm{ZPE}^{\mathrm{gas}} + C_p^{\mathrm{gas}} - TS^{\mathrm{gas}}\right) - \left(\mathrm{ZPE}^{\mathrm{ads}} + C_p^{\mathrm{ads}} - TS^{\mathrm{ads}}\right) \quad (3)$$

where the pH and *U* (in SHE scale) dependent terms are calculated using the computational hydrogen electrode model.[42] The ZPE and thermal contribution terms of adsorbates are obtained from frequency calculations and evaluated at 298.15 K.

A population size of 25 and a mutation rate of 30% are chosen for the GCGA sampling. The pool of initial candidates is generated using the bond length distribution algorithm (BLDA) which is a random structure generation method based on the covalent radii of the atoms.[43] A pre-optimization with Hookean potential is performed to produce reasonable starting geometries before they are fed to electronic structure codes for local optimization and energy evaluation. Mating between the alive candidates to create offspring is done by a split-and-splice operation,[44] in which the parent slabs are cut along a random plane and then spliced together. A fitness factor is assigned to each candidate based on its mating counts and its grand canonical free energy. Candidates with higher fitness (low free energy) are more probable to mate. A similarity check against the current population is performed before adding any new candidate, to prevent duplicates. Adopted mutation operations include: (1) adding or removing an adsorbate, (2) rattling the surface atoms along random vectors drawn from a normal distribution, (3) translating the buffer slab along x or y axis by 1/n (n=2,3,6) of the cell length, (4) permuting a random half of buffer region (original slab and the sampled adsorbates). If an offspring is too similar to its parent, its mutation rate is raised to 100%. Upon the addition of each offspring to the population,

the candidate with the lowest fitness is archived to maintain the population size. The structures with unbound fragments are removed from the population to avoid sampling into chemically irrelevant regions of the PES.

4. Grand canonical DFT calculations.

For the lowest structures in the obtained ensembles, the electrochemical conditions beyond the computational hydrogen electrode (CHE) are applied. Under a constant applied potential, the electrode surface is effectively a grand canonical ensemble of electrons where the number of electrons is varied to adapt to the change in the workfunction of the surface. The potential-dependent electronic grand canonical free energy of the surface Ω_{el} can be approximated by a surface charging model:[45]

$$\Omega_{\mathrm{el}}(U) = E(U) - q(U) \cdot FU \approx E(U_0) - \frac{1}{2}C(U - U_0)^2 \quad (4)$$

which treats the electrochemical interface as an effective capacitor. Here, $E(U)$ is the electronic energy of the surface under a potential U which is calculated by refencing the Fermi level of the system against the vacuum level. $q(U)$ is the surface charge difference referenced against the neutral system, and F is the Faraday constant. U_0 stands for the potential of zero charge in vacuum scale, and C is the effective capacitance.

The self-consistent implicit solvation model VASPsol[46] is used to represent the polarizable electrolyte region. The surface slab is symmetrized along the z-axis to avoid asymmetric potential in the implicit solvation region. The thickness of the implicit solvent slab is increased to 5λ where the Debye screening length is evaluated by:[47]

$$\lambda \approx \frac{3}{\sqrt{I}}\text{Å} \quad (5)$$

where I is the ionic strength in M, in this study we take it to be 0.1 to model the 0.1 M $HClO_4$. Hence the implicit solvent thickness is set to 50 Å for the symmetrized slab (Figure S1c).

By varying the number of electrons in the system, the $E(U)$ of the system at the corresponding U and $q(U)$ can be obtained, and thereby a quadratic relation between $\Omega_{el}(U)$ and U can be fitted by sampling a series of q values. The U (in vacuum scale) can be converted into the SHE scale by referencing it against the benchmarked value (4.60 V for VASPsol).[48]

The final coverage- and potential-dependent grand canonical free energy Ω_{tot} is approximated by:

$$\Omega_{\mathrm{tot}}(n, U) \approx \Omega_{\mathrm{el}}^{\mathrm{slab}-n\mathrm{H}}(U) - \Omega_{\mathrm{el}}^{\mathrm{slab}}(U) - n \cdot \mu_{\mathrm{H}}(\mathrm{pH}, U, T) \quad (6)$$

For consideration of cost, the GCDFT calculations are performed not during the GCGA sampling but on a subset of structures from the final ensemble a posteriori. This approach greatly reduces the computational expense to construct a potential-dependent grand canonical ensemble while capturing the energetics of key accessible states in the ensemble. See benchmarking and justifications in Supplementary Note 2.

5. Monte Carlo simulations.

The evolution of surface adsorbate coverage and configuration under varying potential is studied based on the structures in the ensemble and their potential-dependent free energies, from global optimization and grand canonical DFT calculations. The surface is modeled as a 10×10 lattice, with each grid representing a surface area of the size of the sampling cell.

During each simulation step, two types of moves can be made: (1) Intra-surface exchange, in which one random grid donates a random adsorbate to its neighboring grid; (2) Surface-electrolyte exchange, in which one random grid gains or loses a random adsorbate. The end state of a grid after a move is a randomly selected minimum structure of its corresponding coverage state. The chemical potential of the adsorbate in the reservoir is constant and depends solely on the reaction conditions. The barrier associated with a move is assumed to scale with the change in free energy, which introduces a sense of kinetics into the simulation.

A move is accepted or rejected based on the Metropolis criteria. The temperature of the simulation is set to be 298.15 K, corresponding to room temperature conditions. The system is started at 0.25 V_{RHE} and then varied by 10 mV toward the negative voltage, every 2 million simulation steps. During each phase of the simulated cathodic scan, the system could not reach equilibrium but a quasi-equilibrium corresponding to a metastable regime at that potential. The simulation can hence track the evolution of the kinetically trapped system on a changing free energy landscape and locate its path across the configurational space.

Note that, although the absolute time factor associated with each move is lacking, the simulation should be able to reflect relative time scales at the microsecond level. A rigorous kinetic Monte Carlo set-up would require evaluation of free energy barrier of every possible move in the ensemble, and determination of pre-exponential factors for calculating the rates, which are prohibitively expensive and beyond the scope of this study.

6. Molecular dynamics.

The *ab initio* molecular dynamics simulations are performed on the optimized structures with the same DFT setting as the geometry optimization using the VASP program. The simulation is performed in the NVT (canonical) ensemble at 300 K with the Nose-Hoover thermostat, with a time step of 1 fs. The unconstrained AIMD simulations are performed for more than 20 ps to ensure proper equilibration of the system and to provide initial configurations and velocities for the constrained AIMD simulations to follow.

The slow-growth technique is used to sample the free energy profiles. Specifically, the collective variable (reaction coordinate) corresponding to the studied process is varied very slowly during the sampling, so that all other variables are well equilibrated. The resulting trajectory constitutes a blue moon ensemble and can be used to calculate free energetics by thermodynamic integration. The height of the Cu atom in Cu*CO and the inter-Cu distance are used as the collective variable for the propagation and dimerization, respectively.

ASSOCIATED CONTENT

Supporting Information.

The following files are available free of charge at xxx.

Structural model for GCGA and GCDFT calculations; Statistics of vertical displacement of surface Cu atoms on other facet; Model set-up of the Monte Carlo simulation and the simulated cathodic scan; Evolution of the surface phases under varying potential from the statistics of the Monte Carlo simulation; Chemical bonding analysis of the elevated Cu*CO species; Model set-ups and details of the free energy calculations; Close-up views of the Cu*CO propagation and dimerization processes; Note on the modifications to the GCGA to support polyatomic adsorbates; Note on the details, related timescales, and limitations of the Monte Carlo simulation; Note on chemical bonding analysis of the H-promoted elevation of Cu*CO; Note on details and limitations of the slow-growth MD for free energy profile.

AUTHOR INFORMATION

Corresponding Author

*Corresponding Author's email:

Anastassia N. Alexandrova: ana@chem.ucla.edu

Philippe Sautet: sautet@ucla.edu

Notes

The authors declare no competing financial interest.

ACKNOWLEDGMENTS

The work was supported by the National Science Foundation CBET grant 2103116. Z.Z. was supported by the Dissertation Year Fellowship of UCLA. Computational resources for this work were provided by UCLA shared cluster Hoffman2, and the Innovative and Novel Computational Impact on Theory and Experiment (INCITE) program at the Argonne Leadership Computing Facility, which is a DOE Office of Science User Facility supported under Contract DE-AC02-06CH11357.

REFERENCES

(1) Zhang, Z.; Zandkarimi, B.; Alexandrova, A. N. Ensembles of Metastable States Govern Heterogeneous Catalysis on Dynamic Interfaces. *Acc. Chem. Res.* **2020**, *53* (2), 447–458. https://doi.org/10.1021/acs.accounts.9b00531.

(2) Lavroff, R. H.; Morgan, H. W. T.; Zhang, Z.; Poths, P.; Alexandrova, A. N. Ensemble Representation of Catalytic Interfaces: Soloists, Orchestras, and Everything in-Between. *Chem. Sci.* **2022**, *13* (27), 8003–8016. https://doi.org/10.1039/d2sc01367c.

(3) Nitopi, S.; Bertheussen, E.; Scott, S. B.; Liu, X.; Engstfeld, A. K.; Horch, S.; Seger, B.; Stephens, I. E. L.; Chan, K.; Hahn, C.; Nørskov, J. K.; Jaramillo, T. F.; Chorkendorff, I. Progress and Perspectives of Electrochemical CO2 Reduction on Copper in Aqueous Electrolyte. *Chem. Rev.* **2019**, *119* (12), 7610–7672. https://doi.org/10.1021/acs.chemrev.8b00705.

(4) Piqué, O.; Low, Q. H.; Handoko, A. D.; Yeo, B. S.; Calle-Vallejo, F. Selectivity Map for the Late Stages of CO and CO2 Reduction to C2 Species on Copper Electrodes. *Angew. Chemie Int. Ed.* **2021**, *60* (19), 10784–10790. https://doi.org/https://doi.org/10.1002/anie.202014060.

(5) Dattila, F.; García-Muelas, R.; López, N. Active and Selective Ensembles in Oxide-Derived Copper Catalysts for CO2 Reduction. *ACS Energy Lett.* **2020**, *5* (10), 3176–3184.

(6) Kim, Y. G.; Baricuatro, J. H.; Javier, A.; Gregoire, J. M.; Soriaga, M. P. The Evolution of the Polycrystalline Copper Surface, First to Cu(111) and Then to Cu(100), at a Fixed CO2RR Potential: A Study by Operando EC-STM. *Langmuir* **2014**, *30* (50), 15053–15056. https://doi.org/10.1021/la504445g.

(7) Huang, J.; Hörmann, N.; Oveisi, E.; Loiudice, A.; De Gregorio, G. L.; Andreussi, O.; Marzari, N.; Buonsanti, R. Potential-Induced Nanoclustering of Metallic Catalysts during Electrochemical CO2 Reduction. *Nat. Commun.* **2018**, *9* (1), 3117. https://doi.org/10.1038/s41467-018-05544-3.

(8) Eren, B.; Zherebetskyy, D.; Patera, L. L.; Wu, C. H.; Bluhm, H.; Africh, C.; Wang, L. W.; Somorjai, G. A.; Salmeron, M. Activation of Cu(111) Surface by Decomposition into Nanoclusters Driven by CO Adsorption. *Science.* **2016**, *351* (6272), 475–478. https://doi.org/10.1126/science.aad8868.

(9) Auer, A.; Andersen, M.; Wernig, E. M.; Hörmann, N. G.; Buller, N.; Reuter, K.; Kunze-Liebh user, J. Self-Activation of Copper Electrodes during CO Electro-Oxidation in Alkaline Electrolyte. *Nat. Catal.* **2020**, *3* (10), 797–803. https://doi.org/10.1038/s41929-020-00505-w.

(10) Amirbeigiarab, R.; Tian, J.; Herzog, A.; Qiu, C.; Bergmann, A.; Roldan Cuenya, B.; Magnussen, O. M. Atomic-Scale Surface Restructuring of Copper Electrodes under CO2 Electroreduction Conditions. *Nat. Catal.* **2023**, *6* (9), 837–846. https://doi.org/10.1038/s41929-023-01009-z.

(11) Wan, M.; Yang, Z.; Morgan, H.; Shi, J.; Shi, F.; Liu, M.; Wong, H.-W.; Gu, Z.; Che, F. Enhanced CO2 Reactive Capture and Conversion Using Aminothiolate Ligand–Metal Interface. *J. Am. Chem. Soc.* **2023**, *145* (48), 26038–26051. https://doi.org/10.1021/jacs.3c06888.

(12) Ummireddi, A. K.; Li, Z.; Wu, J. Copper Defects for CO2 Electrocatalysis toward a Specific Multicarbon Product. *Trends Chem.* **2023**, *5* (3), 170–173. https://doi.org/10.1016/j.trechm.2022.12.004.

(13) Zhang, Z.; Wei, Z.; Sautet, P.; Alexandrova, A. N. Hydrogen-Induced Restructuring of a Cu(100) Electrode in Electroreduction Conditions. *J. Am. Chem. Soc.* **2022**, *144* (42), 19284–19293. https://doi.org/10.1021/jacs.2c06188.

(14) Cheng, D.; Wei, Z.; Zhang, Z.; Broekmann, P.; Alexandrova, A. N.; Sautet, P. Restructuring and Activation of Cu(111) under Electrocatalytic Reduction Conditions. *Angew. Chemie - Int. Ed.* **2023**, *62* (20), e202218575. https://doi.org/10.1002/anie.202218575.

(15) Wan, C.; Zhang, Z.; Dong, J.; Xu, M.; Pu, H.; Baumann, D.; Lin, Z.; Wang, S.; Huang, J.; Shah, A. H.; Pan, X.; Hu, T.; Alexandrova, A. N.; Huang, Y.; Duan, X. Amorphous Nickel Hydroxide Shell Tailors Local Chemical Environment on Platinum Surface for Alkaline Hydrogen Evolution Reaction. *Nat. Mater.* **2023**, *22* (8), 1022–1029. https://doi.org/10.1038/s41563-023-01584-3.

(16) Zhang, Z.; Hermans, I.; Alexandrova, A. N. Off-Stoichiometric Restructuring and Sliding Dynamics of Hexagonal Boron Nitride Edges in Conditions of Oxidative Dehydrogenation of Propane. *J. Am. Chem. Soc.* **2023**, *145* (31), 17265–17273.

https://doi.org/10.1021/jacs.3c04613.

(17) Zhang, Z.; Masubuchi, T.; Sautet, P.; Anderson, S. L.; Alexandrova, A. N. Hydrogen Evolution on Electrode-Supported Ptn Clusters: Ensemble of Hydride States Governs the Size Dependent Reactivity. *Angew. Chemie - Int. Ed.* **2023**, *62* (20), e202218210. https://doi.org/10.1002/anie.202218210.

(18) Raciti, D.; Cockayne, E.; Vinson, J.; Schwarz, K.; Hight Walker, A. R.; Moffat, T. P. SHINERS Study of Chloride Order–Disorder Phase Transition and Solvation of Cu(100). *J. Am. Chem. Soc.* **2024**, *146* (2), 1588–1602. https://doi.org/10.1021/jacs.3c11812.

(19) Tackett, B. M.; Raciti, D.; Hight Walker, A. R.; Moffat, T. P. Surface Hydride Formation on Cu(111) and Its Decomposition to Form H2in Acid Electrolytes. *J. Phys. Chem. Lett.* **2021**, *12* (44), 10936–10941. https://doi.org/10.1021/acs.jpclett.1c03131.

(20) Matsushima, H.; Haak, C.; Taranovskyy, A.; Gründer, Y.; Magnussen, O. M. In Situ Video STM Studies of the Hydrogen-Induced Reconstruction of Cu(100): Potential and PH Dependence. *Phys. Chem. Chem. Phys.* **2010**, *12* (42), 13992–13998. https://doi.org/10.1039/c0cp00659a.

(21) Koga, O.; Teruya, S.; Matsuda, K.; Minami, M.; Hoshi, N.; Hori, Y. Infrared Spectroscopic and Voltammetric Study of Adsorbed CO on Stepped Surfaces of Copper Monocrystalline Electrodes. *Electrochim. Acta* **2005**, *50* (12), 2475–2485.

(22) Wuttig, A.; Liu, C.; Peng, Q.; Yaguchi, M.; Hendon, C. H.; Motobayashi, K.; Ye, S.; Osawa, M.; Surendranath, Y. Tracking a Common Surface-Bound Intermediate during CO2-to-Fuels Catalysis. *ACS Cent. Sci.* **2016**, *2* (8), 522–528. https://doi.org/10.1021/acscentsci.6b00155.

(23) Zhan, C.; Dattila, F.; Rettenmaier, C.; Bergmann, A.; Kühl, S.; García-Muelas, R.; López, N.; Cuenya, B. R. Revealing the CO Coverage-Driven C–C Coupling Mechanism for Electrochemical CO2 Reduction on Cu2O Nanocubes via Operando Raman Spectroscopy. *ACS Catal.* **2021**, *11* (13), 7694–7701.

(24) Chorkendorff, I.; Rasmussen, P. B. Reconstruction of Cu(100) by Adsorption of Atomic Hydrogen. *Surf. Sci.* **1991**, *248* (1–2), 35–44. https://doi.org/10.1016/0039-6028(91)90059-2.

(25) Simon, G. H.; Kley, C. S.; Roldan Cuenya, B. Potential-Dependent Morphology of Copper Catalysts During CO 2 Electroreduction Revealed by In Situ Atomic Force Microscopy. *Angew. Chemie Int. Ed.* **2021**, *60* (5), 2561–2568. https://doi.org/10.1002/anie.202010449.

(26) Timoshenko, J.; Bergmann, A.; Rettenmaier, C.; Herzog, A.; Arán-Ais, R. M.; Jeon, H. S.; Haase, F. T.; Hejral, U.; Grosse, P.; Kühl, S.; Davis, E. M.; Tian, J.; Magnussen, O.; Roldan Cuenya, B. Steering the Structure and Selectivity of CO2 Electroreduction Catalysts by Potential Pulses. *Nat. Catal.* **2022**, *5* (4), 259–267. https://doi.org/10.1038/s41929-022-00760-z.

(27) Popović, S.; Smiljanić, M.; Jovanovič, P.; Vavra, J.; Buonsanti, R.; Hodnik, N. Stability and Degradation Mechanisms of Copper-based Catalysts for Electrochemical CO2 Reduction. *Angew. Chemie* **2020**, *132* (35), 14844–14854.

(28) Scholten, F.; Nguyen, K. C.; Bruce, J. P.; Heyde, M.; Roldan Cuenya, B. Identifying Structure–Selectivity Correlations in the Electrochemical Reduction of CO2: A Comparison of Well-Ordered Atomically Clean and Chemically Etched Copper Single-Crystal Surfaces. *Angew. Chemie Int. Ed.* **2021**, *60* (35), 19169–19175.

(29) Kuhl, K. P.; Cave, E. R.; Abram, D. N.; Jaramillo, T. F. New Insights into the Electrochemical Reduction of Carbon Dioxide on Metallic Copper Surfaces. *Energy Environ. Sci.* **2012**, *5* (5), 7050–7059.

(30) Janthon, P.; Luo, S.; Kozlov, S. M.; Viñes, F.; Limtrakul, J.; Truhlar, D. G.; Illas, F. Bulk Properties of Transition Metals: A Challenge for the Design of Universal Density Functionals. *J. Chem. Theory Comput.* **2014**, *10* (9), 3832–3839. https://doi.org/10.1021/ct500532v.

(31) Hammer, B.; Hansen, L. B.; Nørskov, J. K. Improved Adsorption Energetics within Density-Functional Theory Using Revised Perdew-Burke-Ernzerhof Functionals. *Phys. Rev. B - Condens. Matter Mater. Phys.* **1999**, *59* (11), 7413–7421. https://doi.org/10.1103/PhysRevB.59.7413.

(32) Joubert, D. From Ultrasoft Pseudopotentials to the Projector Augmented-Wave Method. *Phys. Rev. B - Condens. Matter Mater. Phys.* **1999**, *59* (3), 1758–1775. https://doi.org/10.1103/PhysRevB.59.1758.

(33) Kresse, G.; Furthmüller, J. Efficiency of Ab-Initio Total Energy Calculations for Metals and Semiconductors Using a Plane-Wave Basis Set. *Comput. Mater. Sci.* **1996**, *6* (1), 15–50. https://doi.org/10.1016/0927-0256(96)00008-0.

(34) Kresse, G.; Furthmüller, J. Efficient Iterative Schemes for Ab Initio Total-Energy Calculations Using a Plane-Wave Basis Set. *Phys. Rev. B - Condens. Matter Mater. Phys.* **1996**, *54* (16), 11169–11186. https://doi.org/10.1103/PhysRevB.54.11169.

(35) Kresse, G. Ab Initio Molecular Dynamics for Liquid Metals. *J. Non. Cryst. Solids* **1995**, *192–193* (1), 222–229. https://doi.org/10.1016/0022-3093(95)00355-X.

(36) Kresse, G.; Hafner, J. Ab Initio Molecular-Dynamics Simulation of the Liquid-Metalamorphous- Semiconductor Transition in Germanium. *Phys. Rev. B* **1994**, *49* (20), 14251–14269. https://doi.org/10.1103/PhysRevB.49.14251.

(37) Henkelman, G.; Uberuaga, B. P.; Jónsson, H. Climbing Image Nudged Elastic Band Method for Finding Saddle Points and Minimum Energy Paths. *J. Chem. Phys.* **2000**, *113* (22), 9901–9904. https://doi.org/10.1063/1.1329672.

(38) Smidstrup, S.; Pedersen, A.; Stokbro, K.; Jónsson, H. Improved Initial Guess for Minimum Energy Path Calculations. *J. Chem. Phys.* **2014**, *140* (21), 214106. https://doi.org/10.1063/1.4878664.

(39) Yu, M.; Trinkle, D. R. Accurate and Efficient Algorithm for Bader Charge Integration. *J. Chem. Phys.* **2011**, *134* (6), 64111. https://doi.org/10.1063/1.3553716.

(40) Otero-De-La-Roza, A.; Johnson, E. R.; Luaña, V. Critic2: A Program for Real-Space Analysis of Quantum Chemical Interactions in Solids. *Comput. Phys. Commun.* **2014**, *185* (3), 1007–1018. https://doi.org/10.1016/j.cpc.2013.10.026.

(41) Sun, G.; Alexandrova, A. N.; Sautet, P. Structural Rearrangements of Subnanometer Cu Oxide Clusters Govern Catalytic Oxidation. *ACS Catal.* **2020**, *10* (9), 5309–5317. https://doi.org/10.1021/acscatal.0c00824.

(42) Yang, T. T.; Patil, R. B.; McKone, J. R.; Saidi, W. A. Revisiting Trends in the Exchange Current for Hydrogen Evolution. *Catal. Sci. Technol.* **2021**, *11* (20), 6832–6838. https://doi.org/10.1039/d1cy01170g.

(43) Zhai, H.; Alexandrova, A. N. Ensemble-Average Representation of Pt Clusters in

Conditions of Catalysis Accessed through GPU Accelerated Deep Neural Network Fitting Global Optimization. *J. Chem. Theory Comput.* **2016**, *12* (12), 6213–6226. https://doi.org/10.1021/acs.jctc.6b00994.

(44) Deaven, D. M.; Ho, K. M. Molecular Geometry Optimization with a Genetic Algorithm. *Phys. Rev. Lett.* **1995**, *75* (2), 288–291. https://doi.org/10.1103/PhysRevLett.75.288.

(45) Steinmann, S. N.; Michel, C.; Schwiedernoch, R.; Sautet, P. Impacts of Electrode Potentials and Solvents on the Electroreduction of CO2: A Comparison of Theoretical Approaches. *Phys. Chem. Chem. Phys.* **2015**, *17* (21), 13949–13963. https://doi.org/10.1039/c5cp00946d.

(46) Mathew, K.; Sundararaman, R.; Letchworth-Weaver, K.; Arias, T. A.; Hennig, R. G. Implicit Solvation Model for Density-Functional Study of Nanocrystal Surfaces and Reaction Pathways. *J. Chem. Phys.* **2014**, *140* (8), 84106. https://doi.org/10.1063/1.4865107.

(47) Steinmann, S. N.; Sautet, P. Assessing a First-Principles Model of an Electrochemical Interface by Comparison with Experiment. *J. Phys. Chem. C* **2016**, *120* (10), 5619–5623. https://doi.org/10.1021/acs.jpcc.6b01938.

(48) Mathew, K.; Kolluru, V. S. C.; Mula, S.; Steinmann, S. N.; Hennig, R. G. Implicit Self-Consistent Electrolyte Model in Plane-Wave Density-Functional Theory. *J. Chem. Phys.* **2019**, *151* (23), 234101. https://doi.org/10.1063/1.5132354.

TOC GRAPHICS